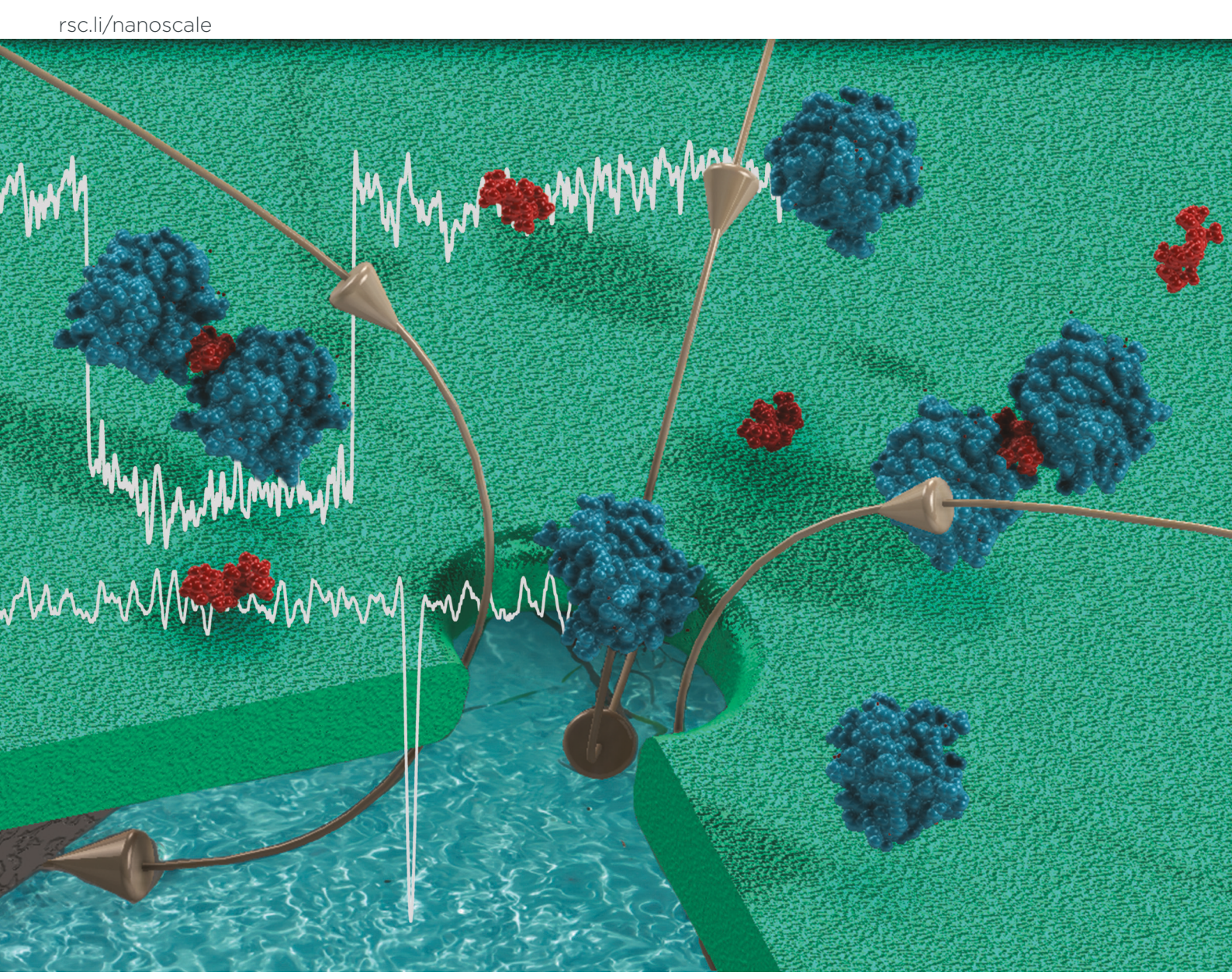
Volume 16 Number 17 7 May 2024 Pages 8179-8674

Nanoscale



ISSN 2040-3372



PAPER

Sangyoup Lee, Min Jun Kim *et al.* Exploring single-molecule interactions: heparin and FGF-1 proteins through solid-state nanopores





PAPER View Article Online
View Journal | View Issue



Cite this: Nanoscale, 2024, 16, 8352

Exploring single-molecule interactions: heparin and FGF-1 proteins through solid-state nanopores†

Navod Thyashan, Da Madhav L. Ghimire, Da Sangyoup Lee*b and Min Jun Kim b*a

Detection and characterization of protein-protein interactions are essential for many cellular processes, such as cell growth, tissue repair, drug delivery, and other physiological functions. In our research, we have utilized emerging solid-state nanopore sensing technology, which is highly sensitive to better understand heparin and fibroblast growth factor 1 (FGF-1) protein interactions at a single-molecule level without any modifications. Understanding the structure and behavior of heparin-FGF-1 complexes at the single-molecule level is very important. An abnormality in their formation can lead to life-threatening conditions like tumor growth, fibrosis, and neurological disorders. Using a controlled dielectric breakdown pore fabrication approach, we have characterized individual heparin and FGF-1 (one of the 22 known FGFs in humans) proteins through the fabrication of 17 + 1 nm nanopores. Compared to heparin, the positively charged heparin-binding domains of some FGF-1 proteins translocationally react with the pore walls, giving rise to a distinguishable second peak with higher current blockade. Additionally, we have confirmed that the dynamic FGF-1 is stabilized upon binding with heparin-FGF-1 at the single-molecule level. The larger current blockades from the complexes relative to individual heparin and the FGF-1 recorded during the translocation ensure the binding of heparin-FGF-1 proteins, forming binding complexes with higher excluded volumes. Taken together, we demonstrate that solid-state nanopores can be employed to investigate the properties of individual proteins and their complex interactions, potentially paving the way for innovative medical therapies and advancements.

Received 18th January 2024, Accepted 17th March 2024 DOI: 10.1039/d4nr00274a

rsc.li/nanoscale

1. Introduction

Nanopore experiments have emerged as powerful tools for single-molecule analysis, enabling the investigation of biomolecules with unprecedented precision. In this study, we focus on heparin, fibroblast growth factor 1 (FGF-1), and their interactions using a solid-state nanopore. Heparin is a polysaccharide known for its unique structural and functional properties. A linear polysaccharide that contains repetitive disaccharide units consisting of uronic acid-(1-4)-p-glucosamine (refer to Fig. 1A) comprises around 70% of the heparin chain making it highly negatively charged. Heparin's negatively charged sulfate groups and flexible molecular structure make

IdoA2S-GlcNS6S

Fig. 1 Molecular structures of (A) heparin and its main disaccharide IdoA2S-GlcNS6S, (B) FGF-1, and (C) the biologically active dimer of the heparin-FGF-1 complex (PDB-1AXM).²⁶ The heparin-binding domains of FGFs, represented by arginine and lysine, are depicted in cyan and lime green, respectively.

it an intriguing candidate for nanopore experiments. This therapeutic agent, discovered in 1916, well-known for its anti-coagulant properties since 1935, is a member of the glycosaminoglycan (GAG) family. Its ability to interact with various

B Heparin

^aDepartment of Mechanical Engineering, Southern Methodist University, Dallas, TX, 75205. USA. E-mail: mikim@lyle.smu.edu

^bBionic Research Center, Biomedical Research Division, Korea Institute of Science and Technology, Seoul, Republic of Korea. E-mail: sangyoup@kist.re.kr

[†]Electronic supplementary information (ESI) available: *I-V* characteristic of nanopores, open pore base line current traces, heparin translocations under different salt conditions, typical current traces of heparin, observation of FGF-1 events at positive and negative voltage biases, FGF-1 current traces in 3 M KCl, heparin-FGF-1 current traces in 3 M KCl, comparison of heparin, FGF-1, and the mixture events at different voltage biases. See DOI: https://doi.org/10.1039/d4nr00274a

biomolecules, including proteins and nucleic acids, has been extensively studied in the context of its role as an anticoagulant and its involvement in cell signalling.³ In particular, its interaction with proteins such as growth factors has been of interest due to its implications for cellular processes. Furthermore, heparin finds extensive applications in various medical contexts. It has been investigated as a potential remedy for inflammatory and allergic disorders.^{4–7} The role of heparin in the treatment of malignancies related to tumours has been thoroughly studied.^{8–10} In addition to its use in countering infections,^{11,12} heparin molecules serve as nanocarriers in drug delivery systems.^{13,14} The highly complex structure of heparin, still under investigation for its exact composition,¹⁵

adds to its diverse range of medical uses.

On the other hand, FGF-1 (refer to Fig. 1B) is one of a family of signalling proteins with around 20 homologues discovered in the human body^{16,17} that play crucial roles in the regulation of cell growth and migration, 18 tissue repair and growth, ¹⁹ wound healing, ^{20,21} angiogenesis, ²² and various physiological and pathological processes. These proteins are dynamic and structurally flexible and modulate specific binding with other proteins such as heparin. They are in high demand as they possess a high affinity for heparin or heparan sulfate proteoglycans (HSPGs) and the significance of the interaction between FGF proteins and these molecules influences a range of regulatory roles, 23 mitogenic activities, 24 cellular activities, signalling pathways, and biomedical applications.25 While the aforementioned mitogenic activities of FGF proteins are intensified by binding to heparin, it has been proven that heparin shields FGF proteins from heat inactivation and proteolytic modifications. 27,28 The binding mechanism involves the formation of a complex between FGF-1 and heparin, impacting FGF-1's conformation and its ability to interact with cell surface receptors. While various homologues of FGF proteins are known to have distinct properties in initiating different physiological processes, here, we delve into an investigation of individual heparin and FGF-1 dynamics, conformation, and heparin-FGF-1 that could help in the understanding in detail of how they collaboratively contribute to essential cellular signalling pathways and biological functions at the single-molecule level.

Despite the numerous advantages associated with interactions with FGFs, it is crucial to acknowledge that the binding of these two molecules may also give rise to negative effects. It has been shown that HSPGs (structurally similar to heparin) play a key role in either facilitating or inhibiting the influence of FGF-2 on tumour cell growth. ²⁹ The complex interplay between the sulfation content of HSPGs and the characteristics of tumour cells is instrumental in determining the contribution of heparin to the influence of FGF on tumour growth. Furthermore, the dysregulation of FGF-1 proteins may lead to various cardiovascular diseases, neurodegenerative disorders, and metabolic disorders. Hence, elucidating the binding kinetics of these two specific proteins has been of paramount importance in the biomedical research sector. While several methodologies have been employed to investi-

gate the structural and binding dynamics of heparin-FGF binding complexes, there is a noticeable absence of research utilizing nanopores for this purpose.

Nanopore sensing, a pioneering single-molecule analysis technique, has earned significant attention and prominence in protein sensing applications since its initial implementation in 1976.³⁰ Compared to other protein analysis techniques, such as X-ray crystallography, nuclear magnetic resonance (NMR), infrared spectroscopy (IR), atomic force microscopy (AFM), *etc.*, nanopore sensing incorporates striking advantages like real-time sensing, label-free analysis, single-molecule detection, versatility, portability, and low sample consumption. Nanopores are mainly of two types: biological nanopores³¹ and solid-state nanopores (SSNs).³² However, there are cases where hybrid nanopores have been used.³³

Biological nanopores offer striking features such as higher precision, selectivity, and biocompatibility. Recent research utilizing biological nanopores has demonstrated their capability to detect protein biomarkers uniquely present in the urine of ovarian cancer patients.³⁴ Furthermore, these nanopores are extensively used in analysing protein conformations and protein–ligand interactions.^{35–37}

SSNs offer distinctive advantages to their biological counterparts like increased stability and throughput, tunability of pore diameter, increased potential of integration with other technologies, and potential of mass production. Chemically tuned solid-state nanopores, a recent advancement in achieving ultra-clean and stable nanopores, have made protein sensing more straightforward and effortless. 38 Today, SSNs are used in a vast scope of applications. Researchers have managed to acquire promising results in the identification of nucleotides within DNA through SSNs. 39,40 The use of nanopores has been extended for diagnostics, 41,42 drug discovery, and biological screening. 43,44 Recent discoveries have demonstrated the real-time monitoring of ion binding to proteins through SSNs. 45 This real-time monitoring capability adds a new aspect to the versatility of SSNs. More importantly, recent research utilizing SSNs has led to insightful breakthroughs in the characterization and discrimination of protein-protein interactions, as well as the identification of biomarkers in disease progression. The characterization and discrimination of amyloid particles through nanopores further extend the scope of disease identification, allowing the observation of disease progression as these particles are identified as biomarkers associated with neurological diseases. 46,47 O'Donohue et al. demonstrated the successful classification of the monomeric and dimeric forms of human serum transferrin receptor proteins through SSNs and confirmed the coexistence of both forms in a heterogeneous mixture.48 The research findings of Yin et al. exemplify the use of nanopores of varying diameters in the discrimination of ferritin and apo-ferritin, which display identical exterior structures and divergent interior structures.49

Thus, it is evident that SSNs can be productively used in discriminating protein–protein interactions. In this research, we will be using nanopores on \sim 12 nm thick silicon nitride

Paper Nanoscale

 (Si_xN_y) membranes to investigate the single-molecule interactions between heparin and FGF-1 proteins. We have characterized individual heparin and FGF-1 proteins through SSNs and observed the binding of heparin and FGF-1 at a singlemolecule level. The findings of this study will shed light on the intricate details of their interactions, providing valuable insights into potential applications in drug discovery and therapeutic interventions. Importantly, this research contributes to the existing body of knowledge, as to the best of our knowledge, no literature has explored the single molecular binding of heparin and FGF-1 proteins through SSNs.

2. Results and discussion

This study employed nanopore technology to perform singlemolecule analyses by quantifying the translocations of individual analytes - heparin, FGF-1, and their complex, heparin-FGF-1 - through a nanopore. The experimental setup is illustrated in Fig. 2. The cis side of the flow cells was loaded with 200 nM analytes, specifically heparin, in electrolytes with varying concentrations of KCl - 1 M, 2 M, and 3 M. This different set of KCl concentrations was used for comparative analysis at various potential biases ranging from 100 mV to 400 mV. Under the influence of an applied positive potential, the transport of analytes across the nanopore results in transient current blockades, as depicted in the bottom panel of each cartoon. The typical current-time traces (t = 0.5 s), represented below each cartoon, were recorded with 3 M KCl electrolytes under a +200 mV potential. The same experimental protocol was applied to investigate FGF-1 (Fig. 2B) and the heparin-FGF-1 complex (Fig. 2C). The experimental setup and methodology were consistent across all three scenarios (heparin, FGF-1, and heparin-FGF-1), providing a systematic approach to

observe and investigate their properties deciphering the translocating events using nanopore technology.

The detectability of heparin through solid-state nanopores under electrolyte concentrations of 1 M KCl has been empirically established by researchers. Notably, experimental observations suggest that an increase in both current blockades and event frequency is associated with heparin translocations at higher electrolyte molarities.⁵⁰ Consequently, heparin translocations were systematically investigated across 3 distinct electrolyte molarities, namely 1 M KCl, 2 M KCl, and 3 M KCl. The outcomes of these investigations as outlined in section 3 of the ESI (Fig. S3A-D†) supported the aforementioned observations by researchers, proving the amplification of heparin capture rates and event blockades under elevated electrolyte molarities. After the initial investigation, an in-depth exploration of heparin translocations was initiated under the conditions of 3 M KCl utilizing a nanopore characterized by a diameter of 17.5 nm \pm 0.9 nm. The pore fabrication was carried out following the pore fabrication protocol detailed in the Experimental section. The open-pore current traces for the voltages 100 mV, 200 mV, 300 mV, and 400 mV as outlined in section 2 of the ESI (Fig. S2†) displayed very stable currents with minimum noise and fluctuations. Baseline currents of this nature are sought in nanopore analysis, as elevated noise and fluctuations have the potential to impede the clear detection of current drops attributed to the translocation of analytes. Moreover, these transient current waveforms suggest that the pore is not uniform and might contain residuals within the pore. Fig. 3A illustrates 0.5 s current traces of heparin at specific voltage biases of 100 mV, 200 mV, 300 mV, and 400 mV. As elaborated on in section 4 of the ESI (Fig. S4†), although heparin translocations displayed clean spikes in the current traces, they displayed a low signal-to-noise ratio.

Heparin is considered to be a polyanionic substance with the highest negative charge density of any known biological

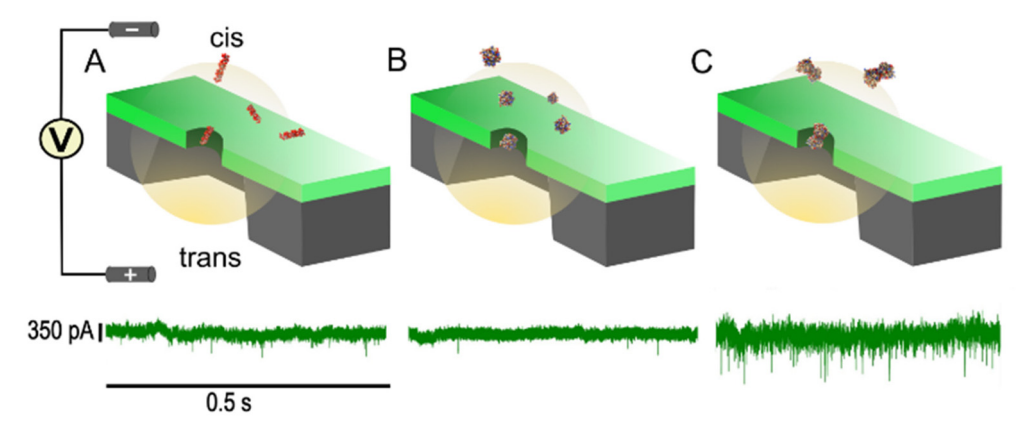


Fig. 2 Schematic representations of nanopore experimental configurations displaying the translocation of proteins through an approximately 17 nm nanopore. (A) Translocation of heparin from the cis side to the trans side of the flow cell. (B) Translocation of heparin fibroblast growth factor 1 (FGF-1) from the cis side to the trans side of the flow cell, and (C) a mixture of heparin and fibroblast growth factor 1 in a 1:1 ratio translocating through the pore. The real-time current traces (t = 0.5 s) for each scenario are represented just below the respective cartoon representations and were taken at +200 mV. All the data used in this research were collected under 100 mV, 200 mV, 300 mV, and 400 mV applied transmembrane potentials in 3 M KCl at pH 7.6. The concentration of the proteins was maintained at 200 nM in the electrolytes for the experiments.

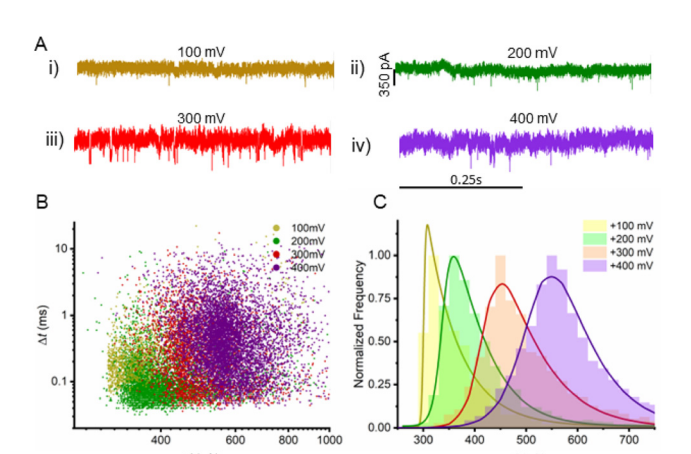


Fig. 3 Translocation dynamics of heparin (15.7 kDa) through an \sim 17 nm nanopore in a 12 nm thick Si_xN_y membrane. The *cis* and *trans* chambers are filled with symmetric 3 M KCl and 10 mM TRIS electrolyte at pH 7.6, and 200 nM heparin was added to the *cis* side. (A) Sample current traces of heparin at various applied transmembrane potentials: (i) 100 mV (bronze), (ii) 200 mV (green), (iii) 300 mV (red), and (iv) 400 mV (purple). Each trace is of t=0.5 s. (B) Scatter plot of dwell time (Δt) vs. current blockade (Δl) at the applied potentials of 100 mV, 200 mV, 300 mV, and 400 mV. (C) Distribution of current blockades for all translocation events of heparin at different applied potentials ranging from 100 mV to 400 mV. The Δl values (mean) obtained from the fit were 341.5 pA (n=10.8), 338.8 pA (n=4930), 420.5 pA (n=2886), and 519.3 pA (n=6495) at 100 mV, 200 mV, 300 mV, and 400 mV, respectively. The data in the distribution are represented by the colored bars, while the solid line with the same color is their fit.

macromolecule.⁵¹ This negative charge is typically due to the presence of negatively charged sulfate and carboxyl groups. The main disaccharide unit (IdoA,2S–GlcNS,6S) of high-grade heparin used in our experiments comprises two sulfate groups and a carboxyl group from the iduronic acid. While it may not be possible to confirm the state of neutrality of such polyanionic molecules, it is noteworthy that heparin could be highly negative at the physiological pH 7.6. The observed low signal-to-noise ratio finds justification in the electrostatic interactions between heparin and the nanopore wall. Heparin, which is recognized for its extreme structural variability,⁵¹ exhibits flexibility and conformational changes during translocations, which cause heightened noise.

Furthermore, heparin's known hydrophilicity and its capacity to retain approximately 2–10% water even after thorough desiccation 52,53 may result in a larger and more dynamic hydrating shell, introducing additional noise into the system. The illustrated trends in current blockade (ΔI) and dwell time (Δt) in Fig. 3B reveal an increasing trend in both parameters with increasing voltage. This implies that heparin undergoes conformational changes, potentially unfolding at higher electrophoretic forces. Fig. 3C and the summarized data under Table 1 highlight the escalating trend in mean current blockades of heparin translocations in response to increasing voltage biases of +100 mV, +200 mV, +300 mV, and +400 mV, respectively. This observation aligns with Ohm's law, which suggests an anticipated elevation in current drop for a

Table 1 The mean current blockade values for the three analytes, heparin (200 nM), FGF-1 (200 nM), and their mixture (heparin 100 nM + FGF-1 100 nM), under different voltage biases. Bimodal peaks were observed under FGF-1, and the mean current blockade values are summarized

	Transmembrane potential (mV)			
Analyte	+100	+200	+300	+400
Heparin $(\Delta I/pA)$	300.7	338.9	420.5	519.3
FGF-1 $(\Delta I/pA)$	276.6, 538.2	292.2, 848.7	382.3, 1097.7	501.7, 777.5
Mixture $(\Delta I/pA)$	1426.5	1686.6	2763.6	_

constant resistance (which arises from the pore) with increasing voltage.

In addition, we analyzed the behaviour of FGF-1 events as proteins translocated through a chemically tuned controlled dielectric breakdown (CT-CDB) pore with a diameter of 17.2 nm ± 1.0 nm in the presence of 3 M KCl. The literature suggests that FGF-1 proteins have an isoelectric point (pI) of 7.54 Notably, at our experimental pH of 7.6, translocations at positive voltage biases were observed, confirming that FGF-1 maintained a net negative charge even under these experimental conditions (see ESI: Fig. S5A and B†). The three-dimensional structure of FGF-1 proteins comprises lysine at heparin-binding domains. Previous site-directed mutagenesis studies and the X-ray crystal structure of FGF-1 have emphasized the significance of these positively charged lysine residues in heparin binding and other biological functions. ⁵⁵⁻⁵⁸

Moreover, studies have confirmed the presence of arginine residues in FGF-1, which are positively charged and contribute to the binding of heparin.⁵⁹ FGF-1 events displayed bimodal distributions of current blockades (Fig. 4C), with the first peak comparable to that of the heparin mean current blockade and the second peak significantly higher in magnitude than that of heparin. Fig. S6 under section 6 of the ESI† elaborates a detailed comparative study of these two types of peaks along the transmembrane voltages: +100 mV, +200 mV, +300 mV, and +400 mV. Summarized in Table 1 are the mean current drops of these bimodal distributions observed in FGF-1 events. We hypothesize that the interaction of these positively charged domains of FGF-1 at the physiological pH with the negatively charged nanopore walls may result in higher blockades during their translocation. The opposite charge attraction forces between the heparin-binding domains of FGF-1 molecules and nanopore walls attract the molecules towards the pore walls during their translocation. This introduces non-uniformity in the electric field inside the nanopore and results in a considerable change in ionic resistance while FGF-1 diffuses through the orifice. The off-axis effects⁶⁰ or the temporal change in resolution⁶¹ that ensue could lead to the bimodal blockade distributions observed during FGF-1 translocations. The transient spikes, as seen in the current traces of 0.5 s (Fig. 4A), result from the passage of FGF-1 through the pore. The relationship

Paper Nanoscale

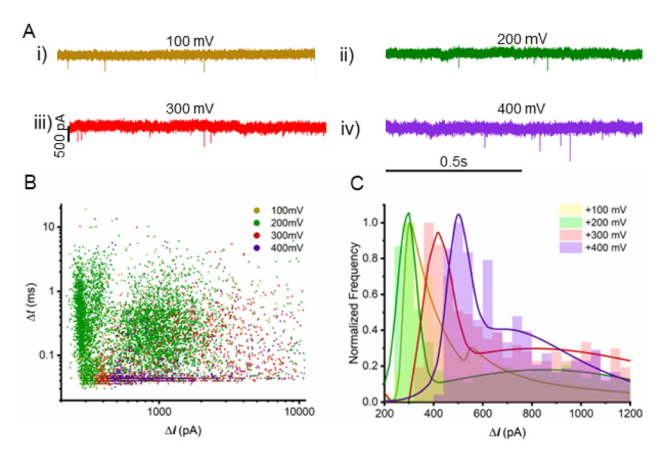


Fig. 4 Translocation dynamics analysis of fibroblast growth factor 1 (FGF-1) through an ~17 nm nanopore in a 12 nm thick Si_xN_y membrane. The cis and trans chambers are filled with symmetric 3 M KCl and 10 mM TRIS electrolytes at pH 7.6. The cis side was loaded with 200 nM FGF-1 at room temperature. (A) Sample current traces of FGF-1 at various applied transmembrane potentials: (i) 100 mV (bronze), (ii) 200 mV (green), (iii) 300 mV (red), and (iv) 400 mV (purple). Each trace is of t = 1 s. (B) Scatter plot of dwell time (Δt) vs. current blockade (Δl) at the applied potentials of 100 mV, 200 mV, 300 mV, and 400 mV. (C) Statistical representation of the current blockade distribution of translocation events ranging from 100 mV to 400 mV. The ΔI values (mean) of the first peak obtained from the fit were 276.6 pA (n = 1157), 292.2 pA (n = 1157), 29 = 5515), 382.3 pA (n = 1033), and 501.7 pA (n = 575) at 100 mV, 200 mV, 300 mV, and 400 mV, respectively. 'n' is the number of extracted events used for data analysis. The data in the distribution are represented by the colored bars, while the solid line with the same color is their fit. Note that the FGF-1 current blockade distribution exhibits a bimodal pattern, unlike the previously illustrated heparin distribution. The second peak was observed at 848.688 pA, 1097.744 pA, and 777.471 pA at 200 mV, 300 mV, and 400 mV, respectively. In contrast to heparin events, FGF-1 proteins exhibited clean translocations across the range of applied voltages, as illustrated in Fig. 4A. Unlike heparin, FGF-1 displayed bimodal peaks of current blockades at +200 mV, +300 mV, and +400 mV, as shown in Fig. 4C. Two distinct regions of FGF-1 events at +200 mV are visible in Fig. 4B. These observations can be rationalized by considering the structural configuration of FGF-1.

between dwell time and the corresponding current blockades as a function of applied positive potential is depicted in a scatter plot (Fig. 4B).

Extensive research has conclusively demonstrated the formation of dimeric complexes involving FGF-1, their receptors and heparin, unravelling how FGF-1 effectively binds with heparin even in the absence of its receptors.⁶² Though it has been well established that sulfate and carboxylate groups within heparin chains play a crucial role in interacting with FGF-1 heparin-binding domains through direct ionic interactions, 63 it is noteworthy to understand the contribution of optimal van der Waals forces in strengthening the heparin-FGF-1 binding complex.⁶⁴ Moreover, the specificity of FGF-1 serotype binding to heparin is highlighted by the unique sulfate requirements. Unlike most FGF serotypes that require only one sulfate (2-O sulfation), the FGF-1 serotype necessitates both the 2-O sulfate and 6-O sulfate of heparin disaccharide for efficient binding.65 Consequently, it can be reasoned that the two samples, heparin and FGF-1, used in our study bound directly and efficiently when mixed and incubated.

Previous research has confirmed the biologically active dimeric structure of the heparin-FGF-1 binding complex, as illustrated in Fig. 1C.26 Our molecules of interest, heparin and FGF-1, naturally adapt a stable conformation. However, external forces generated from the enhanced electric field in the pore's vicinity could facilitate conformational changes within their structures. These conformational changes have the potential to form alternative complexes with more than two FGF-1 proteins bound to heparin. The above reasoning is supported by the significant increase in current drops observed in the translocation of the mixture. Fig. 5A shows the increase in blockade amplitude when compared to individual heparin and FGF-1 events. As depicted in Fig. 5C, there is an approximately 5-fold increase in the mean current drop at voltages +100 mV, +200 mV, and +300 mV. However, the signal-to-noise ratio is notably low compared to that of individual analyte translocations, and frequent clogging events were encountered in mixture translocations suggesting that the complex is more stable than the individual analytes. Moreover, single events displayed either two-step current drops or current drops with higher dwell times (see ESI Fig. S7A-D†). This can be attributed to the different orientations and conformations of heparin-FGF-1 complexes translocated through the nanopore. Presumably, the binding of heparin with FGF-1 stabilizes the structure, restricting the FGF-1 flexibility. The overall charge of

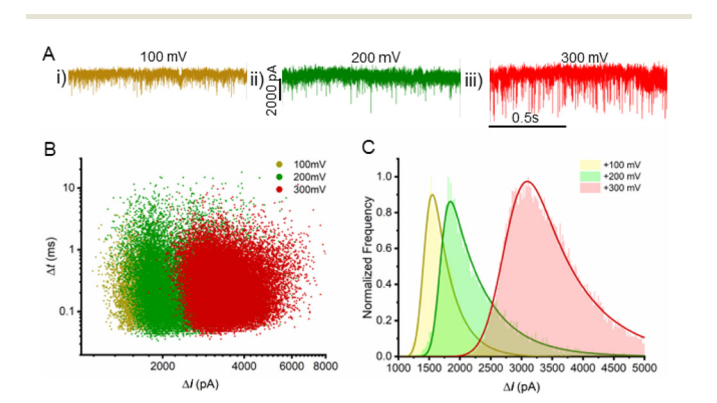


Fig. 5 Mixture analysis for heparin and FGF-1 proteins. 100 nM highgrade heparin (HGH) is mixed with 100 nM FGF-1 in an equal ratio (1:1) before loading to the cis side for studying translocation dynamics. The cis and trans chambers are filled with symmetric 3 M KCl and 10 mM TRIS salt concentrations at pH 7.6. A 100 nM equimolar mixture was loaded to the cis side before taking measurements. (A) Sample current traces of heparin + FGF-1 at various applied transmembrane potentials: (i) 100 mV (bronze), (ii) 200 mV (green), and (iii) 300 mV (red). Each trace is of t = 1 s. (B) Scatter plot of dwell time (Δt) vs. current blockade (Δl) under an applied potential of 100 mV-300 mV. (C) Statistical representation of the current blockade distribution of translocation events ranging from 100 mV to 300 mV. The ΔI values (mean) obtained from the fit were 1426.4 pA (n = 1266), 1686.6 pA (n = 3850), and 2763.6 pA (n = 2302) at 100 mV, 200 mV, and 300 mV, respectively. 'n' is the number of extracted events used for data analysis. The data in the distribution are represented by the colored bars, while the solid line with the same color is their fit.

heparin molecules remains mostly unchanged after binding with FGF-1 proteins, as heparin is inherently considered a highly sulphated and highly negatively charged molecule. The translocation of binding complexes, which are highly negatively charged, through a negatively charged pore gives rise to electrostatic repulsions. These repulsions can induce fluctuations in ion transport through the nanopore, ultimately manifesting as elevated noise in the current signal during experiments. As discussed earlier, the heightened noise levels can be attributed to the electrostatic interactions between the binding complexes and the negatively charged pore membrane. Furthermore, the frequent clogging events resemble the augmentation of the excluded volume of translocated analytes (mixture) compared to the individual heparin FGF-1 molecules. It is noteworthy that unbound heparin and FGF1 molecules could be translocating through the nanopore. However, the higher noise associated with complex translocations is significantly greater than that of blockades linked to individual heparin and FGF1 translocations. Thus, these elevated noise levels could impede the detection of such translocations. Fig. 5B illustrates a scatter plot depicting the translocating complex characteristics confirming a rise in both the dwell time and blockades as the applied potential increases from 100 mV to 300 mV.

To acquire a better picture, we have compared the individual heparin, and FGF-1 events and the mixture events under a +200 mV voltage bias in a 3 M KCI electrolyte. Thousands of events were analyzed, and the results are plotted in Fig. 6A as a scatter plot of dwell time vs. current blockades. Each dot represents a single event. As evident from Fig. 6B, the current distribution appears to be unique and there is a distinguishable

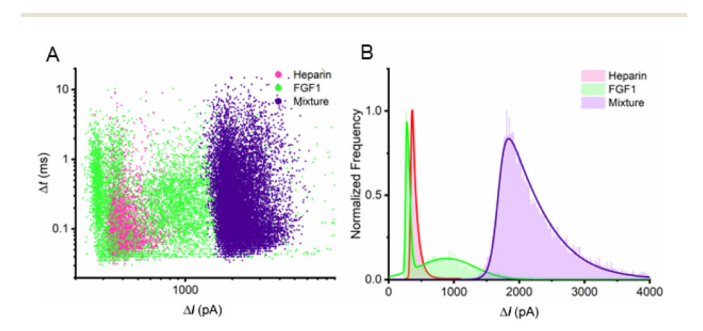


Fig. 6 Comparison of translocation dynamics of heparin (pink), FGF-1 (green), and the heparin-FGF-1 complex (purple) under consistent 3 M KCl, 10 mM TRIS, pH 7.6 electrolytic conditions and applied transmembrane potential. Heparin and FGF-1 were mixed in an equal ratio (1:1) in the same electrolyte before loading to the cis side of the flow cell before taking experimental data. (A) Scatter plot of dwell time (Δt) vs. current blockade (ΔI) at an applied potential of 200 mV. (B) The current blockades distribution of translocation events at 200 mV. The data in the distribution are represented by the colored bars, while the solid line with the same color is their fit. The ΔI values (mean) obtained from the fit were 338.8 pA (n = 4930), 292.2 pA (n = 5515), and 1686.593 pA (n = 5515) 3850) for heparin, FGF-1, and the mixture. 'n' is the number of extracted events used for data analysis. Both the mixture blockade events at +200 mV are distinctive against the heparin and FGF-1 events, giving rise to a 5-fold increase in current drop compared to individual heparin and FGF-1 translocations.

increase in the blockade distribution of the mixture compared to that of individual heparin and FGF-1. Similar types of relationships are seen at other voltages as summarized in the ESI (Fig. S8A-C†). These observations suggest that solid-state nanopore systems can be efficiently utilized to discriminate between individual heparin and FGF-1 and their binding complexes - which is essential for understating their biophysical properties that can influence various biological activities. In contrast to alternative methods like X-ray crystallography, nuclear magnetic resonance (NMR), infrared spectroscopy (IR), and atomic force microscopy (AFM) used for comprehending protein-protein interactions, nanopore technology addresses challenges such as the elevated cost of reagents and devices and the time-scale required for analysis.

3. Conclusions

Protein-protein interactions (PPIs) play an important role in various biological processes, and their significance extends across different aspects of cellular function. In this study, nanopore technology was employed to investigate the properties of heparin, FGF-1, and their complex, heparin-FGF-1 interactions at a single-molecule level. The distinct patterns observed in the translocations of individual analytes and their binding complexes highlight the potential for discriminating between heparin, FGF-1, and their interactions. The observed trends in current blockades and dwell time of heparin translocation suggested conformational changes in heparin, potentially unfolding at higher electrophoretic forces. Similar experiments were conducted for FGF-1, and the results indicated bimodal distributions of current blockades, possibly associated with the electrostatic interactions between FGF-1 and the nanopore walls. The study also explored the mixture of heparin and FGF-1 (1:1), revealing a 5-fold increase in blockade amplitude compared to individual analyte events confirming the formation of the heparin-FGF-1 complex. This has allowed us to monitor the heparin-FGF-1 interactions in a very rapid fashion in a real-time scenario. To thoroughly evaluate the accuracy of their discrimination, future work will involve comparing the histogram with a theoretical distribution curve, applying numerical simulations to assess their alignment. However, multicomponent transient complexes have yet to be characterized in terms of their detailed structures and binding affinity. This research opens avenues for further exploration and refinement of nanopore technology in the analysis of protein-protein interactions. Future studies could delve deeper into understanding the molecular mechanisms governing these translocations, particularly focusing on the conformational changes and structural stability of the heparin-FGF-1 complex. Exploring the specificities of FGF-1 serotype binding to heparin, as well as the role of van der Waals forces in strengthening the complex, could provide valuable insights into the binding dynamics. Additionally, efforts to optimize experimental conditions and nanopore characteristics may enhance the sensitivity and specificity of the technique.

Paper Nanoscale

Ultimately, the ability to discriminate and characterize these molecular interactions at the single-molecule level holds significant promise for modulating the biological activity of FGF-1, offering potential applications in therapeutic and drug development.

Experimental 4.

Materials

 Si_rN_v membranes of ~12 nm thickness were directly purchased from Norcada (NXDB-50H105V122) for nanopore fabrication. Nanopore fabrication on Si_xN_v membranes was achieved through CT-CDB.66 SixNv chips were loaded between two polydimethylsiloxane (PDMS) layers and encapsulated within two flow cells. Subsequently, the two flow cell chambers were filled with 370 μ l of 10 mM tris-buffered 1 M KCl at pH 10.0 and 80 µl of NaOCl (product number: 425044, Sigma-Aldrich) each. A pore (<17 nm) was initially fabricated by applying 7 V-8 V across the membrane. The targeted pore diameter of ~17 nm was achieved by applying voltage pulses at 4.5 V, with periodic monitoring of pore diameter conducted by analyzing the pore's current-voltage (I-V) characteristic curve with a 1 kHz low-pass Bessel filter. The final current-voltage characteristic curves are outlined in section 1 under the ESI (Fig. S1A and B†). Post-pore fabrication, the flow-cell setup underwent meticulous cleaning employing deionized (DI) water to eliminate residual bleach contaminants. For regulating pH in our electrolytes, HCl (product number: 1.60328, Sigma-Aldrich) and KOH (product number: 1.09107, Sigma-Aldrich) were used.

Sample preparation

50 μM stock solutions of high-grade heparin (HEP-HG 100, Iduron, UK) were prepared by dissolving 11.8 mg of solid (as supplied) in 15 ml of >18 MΩ cm ultra-pure water (ARS-102 Aries High-Purity Water Systems). 6.45 µM stock solutions of E. coli-derived human fibroblast growth factor acidic/FGF-1 (CQ3622021, Bio-Techne, USA) were prepared by dissolving 25 μg of protein in 250 μl of 1× PBS (phosphate-buffered saline). For all sets of experiments, KCl was used as the electrolyte. KCl (P9333, Sigma-Aldrich) was prepared by dissolving the required amount of salt in ultra-pure water and buffering using a 10 mM TRIS buffer (J61036, Fisher Scientific, USA). The required pH was achieved by appropriately adding 1 M HCl or 1 M KOH droplets and taking frequent pH measurements using an Orion Star pH/conductivity multiparameter meter.

Nanopore sensing setup and methodology

For protein-sensing experiments, cis and trans chambers were filled with 450 µl of 10 mM tris-buffered 3 M KCl at pH 7.6. Prior to the introduction of any analyte to the flow cell, openpore currents were recorded with a 10 kHz low-pass Bessel filter at 4 different voltage biases, 100 mV, 200 mV, 300 mV, and 400 mV, and all analytes were brought down to room

temperature and were sonicated for 15 min in an ultrasonic bath (CPX2800H BRANSON series). In the context of individual heparin experiments, heparin was introduced to the cis chamber to a final concentration of 200 nM and subsequently translocated through the nanopore to the trans chamber under distinct voltage biases of 100 mV, 200 mV, 300 mV, and 400 mV. Correspondingly, this protocol was applied to individual FGF-1 experiments. Heparin-FGF-1 binding complexes were prepared by mixing 100 nM of heparin and FGF-1 each and were incubated (BIO-RAD T100 Thermal Cycle) at 37 °C for 1 hour.

Data analysis

The electrical measurements in the sets of experiments were conducted using an Axopatch 200B amplifier (Molecular Devices, LLC) with a low-pass Bessel filter at 10 kHz sampled at 250 kHz and digitized using an Axon Digidata 1550B system (Molecular Devices, LLC). Data were recorded with pCLAMP 11.2 software (Molecular Devices). All the recorded event profiles were extracted using EventPro 3 software, 67 and the data were further analyzed using OriginPro 2024 version 10.1.0.170 (OriginLab Corporation) software.

Author contributions

The research idea was developed by N. T., M. L. G., S. L., and M. J. K. The methodology and experiments were conducted by N. T. The data were analyzed by N. T. and M. L. G. The project and research were supervised by S. L. and M. J. K. The manuscripts were written and edited by N. T., M. L. G., S. L., and M. J. K.

Conflicts of interest

There are no conflicts to declare.

Acknowledgements

This work was supported by the National Science Foundation (CBET #2022374 and CBET #2041340), the Ministry of Education and ICT through the National Research Foundation of Korea (RS-2023-00259957), and the Korea Institute of Science and Technology Institutional Program (2E32341). The authors would also like to acknowledge the support of Madhav Ghimire for conceptualizing and designing the project and Matthew O'Donohue and Kamruzzaman Joty for their insightful discussion and technical support.

References

- 1 J. Mclean, Circulation, 1959, 19, 75-78.
- 2 D. A. Lane and U. Lindahl, Heparin: chemical and biological properties, clinical applications, CRC press, Boca Raton (Fla.), 1989.

3 A. R. Rezaie and H. Giri, *J. Thromb. Haemostasis*, 2020, **18**, 3142–3153

- 4 L. Litov, P. Petkov, M. Rangelov, N. Ilieva, E. Lilkova, N. Todorova, E. Krachmarova, K. Malinova, A. Gospodinov, R. Hristova, I. Ivanov and G. Nacheva, *Int. J. Mol. Sci.*, 2021, 22, 10730.
- 5 L. J. Downing, R. M. Strieter, A. M. Kadell, C. A. Wilke, L. J. Greenfield and T. W. Wakefield, *J. Vasc. Surg.*, 1998, 28, 848–854.
- 6 S. Mousavi, M. Moradi, T. Khorshidahmad and M. Motamedi, *Adv. Pharmacol. Sci.*, 2015, 2015, 1–14.
- 7 A. Fal, J. Allergy Clin. Immunol., 2004, 113, S36.
- 8 S. Mousa and L. Petersen, *Thromb. Haemostasis*, 2009, **102**, 258–267.
- 9 R. Lokwani, N. S. Azmi, M. Mohd Yusoff and S. J. A. Ichwan, *J. Biochem. Microbiol. Biotechnol.*, 2014, 2, 76–82.
- 10 J.-H. Lee, S.-B. Yang, J.-H. Lee, H. Lim, S. Lee, T.-B. Kang, J.-H. Lim, Y. J. Kim and J. Park, *Carbohydr. Polym.*, 2023, 314, 120930.
- 11 B. G. Ivan Fernandez Vega, *J. Med. Microbiol. Diagn.*, 2014, 3, 1000157.
- 12 J. Liu, Z. Shriver, R. M. Pope, S. C. Thorp, M. B. Duncan, R. J. Copeland, C. S. Raska, K. Yoshida, R. J. Eisenberg, G. Cohen, R. J. Linhardt and R. Sasisekharan, J. Biol. Chem., 2002, 277, 33456–33467.
- 13 Y.-I. Chung, J. C. Kim, Y. H. Kim, G. Tae, S.-Y. Lee, K. Kim and I. C. Kwon, *J. Controlled Release*, 2010, **143**, 374–382.
- 14 X. Yang, H. Du, J. Liu and G. Zhai, *Biomacromolecules*, 2015, 16, 423-436.
- 15 Y. Ouyang, L. Yi, L. Qiu and Z. Zhang, *Chin. J. Chromatogr.*, 2023, 41, 107–121.
- 16 M.-H. Xie, I. Holcomb, B. Deuel, P. Dowd, A. Huang, A. Vagts, J. Foster, J. Liang, J. Brush, Q. Gu, K. Hillan, A. Goddard and A. L. Gurney, *Cytokine*, 1999, 11, 729–735.
- 17 C. Koga, N. Adati, K. Nakata, K. Mikoshiba, Y. Furuhata, S. Sato, H. Tei, Y. Sakaki, T. Kurokawa, K. Shiokawa and K. K. Yokoyama, *Biochem. Biophys. Res. Commun.*, 1999, 261, 756-765.
- 18 R. Tsuboi, Y. Sato and D. B. Rifkin, *J. Cell Biol.*, 1990, **110**, 511–517.
- 19 M. Farooq, A. W. Khan, M. S. Kim and S. Choi, *Cells*, 2021, 10, 3242.
- 20 Y. Koike, M. Yozaki, A. Utani and H. Murota, *Sci. Rep.*, 2020, **10**, 18545.
- 21 S. Dolati, M. Yousefi, A. Pishgahi, S. Nourbakhsh, B. Pourabbas and S. K. Shakouri, *Growth Factors*, 2020, **38**, 25–34.
- 22 E. J. Battegay, J. Mol. Med., 1995, 73, 333-346.
- 23 R. Sasisekharan, S. Ernst and G. Venkataraman, *Angiogenesis*, 1997, **1**, 45–54.
- 24 G. Gimenez-Gallego, G. Conn, V. B. Hatcher and K. A. Thomas, *Biochem. Biophys. Res. Commun.*, 1986, 138, 611–617.
- 25 M. Zakrzewska, E. Marcinkowska and A. Wiedlocha, *Crit. Rev. Clin. Lab. Sci.*, 2008, **45**, 91–135.

- 26 A. D. DiGabriele, I. Lax, D. I. Chen, C. M. Svahn, M. Jaye, J. Schlessinger and W. A. Hendrickson, *Nature*, 1998, 393, 812–817.
- 27 D. Gospodarowicz and J. Cheng, J. Cell. Physiol., 1986, 128, 475–484.
- 28 T. K. Rosengart, W. V. Johnson, R. Friesel, R. Clark and T. Maciag, *Biochem. Biophys. Res. Commun.*, 1988, 152, 432– 440.
- 29 M. Delehedde, E. Deudon, B. Boilly and H. Hondermarck, *Exp. Cell Res.*, 1996, 229, 398–406.
- 30 E. Neher and B. Sakmann, Nature, 1976, 260, 799-802.
- 31 J. W. F. Robertson, M. L. Ghimire and J. E. Reiner, *Biochim. Biophys. Acta, Biomembr.*, 2021, **1863**, 183644.
- 32 L. Xue, H. Yamazaki, R. Ren, M. Wanunu, A. P. Ivanov and J. B. Edel, *Nat. Rev. Mater.*, 2020, 5, 931–951.
- 33 N. A. W. Bell and U. F. Keyser, *FEBS Lett.*, 2014, **588**, 3564–3570.
- 34 T. W. Rockett, M. Almahyawi, M. L. Ghimire, A. Jonnalagadda, V. Tagliaferro, S. J. Seashols-Williams, M. F. Bertino, G. A. Caputo and J. E. Reiner, ACS Sens., 2024, 9, 860–869.
- 35 X. Li, K. H. Lee, S. Shorkey, J. Chen and M. Chen, ACS Nano, 2020, 14, 1727–1737.
- 36 N. S. Galenkamp, M. Soskine, J. Hermans, C. Wloka and G. Maglia, *Nat. Commun.*, 2018, 9, 4085.
- 37 S. Zernia, N. J. Van Der Heide, N. S. Galenkamp, G. Gouridis and G. Maglia, *ACS Nano*, 2020, **14**, 2296–2307.
- 38 J. Saharia, Y. M. N. D. Y. Bandara, B. I. Karawdeniya, J. R. Dwyer and M. J. Kim, *Small*, 2023, 19, 2300198.
- 39 H. Yamazaki, R. Hu, Q. Zhao and M. Wanunu, *ACS Nano*, 2018, **12**, 12472–12481.
- 40 R. Akahori, I. Yanagi, Y. Goto, K. Harada, T. Yokoi and K. Takeda, *Sci. Rep.*, 2017, 7, 9073.
- 41 S. Cai, J. Y. Y. Sze, A. P. Ivanov and J. B. Edel, *Nat. Commun.*, 2019, **10**, 1797.
- 42 J. Y. Y. Sze, A. P. Ivanov, A. E. G. Cass and J. B. Edel, *Nat. Commun.*, 2017, **8**, 1552.
- 43 M. L. Ghimire, D. R. Gibbs, R. Mahmoud, S. Dhakal and J. E. Reiner, *Anal. Chem.*, 2022, **94**, 10027–10034.
- 44 M. L. Ghimire, B. D. Cox, C. A. Winn, T. W. Rockett, N. P. Schifano, H. M. Slagle, F. Gonzalez, M. F. Bertino, G. A. Caputo and J. E. Reiner, ACS Nano, 2022, 16, 17229– 17241.
- 45 M. O'Donohue, M. L. Ghimire, S. Lee and M. J. Kim, *J. Chem. Phys.*, 2024, **160**, 044906.
- 46 J. Houghtaling, J. List and M. Mayer, *Small*, 2018, **14**, 1802412.
- 47 L. Zhan, T. Jin, J. Zhou, W. Xu, Y. Chen and R. Mezzenga, *Nano Lett.*, 2023, **23**, 9912–9919.
- 48 M. O'Donohue, J. Saharia, N. Bandara, G. Alexandrakis and M. J. Kim, *Electrophoresis*, 2023, 44, 349–359.
- 49 Y.-D. Yin, F.-F. Chen, J. Hu, L. Yang, X.-T. Song, G.-R. Wu, M. Xu and Z.-Y. Gu, Anal. Chem., 2023, 95, 16496–16504.
- 50 B. I. Karawdeniya, Y. M. N. D. Y. Bandara, J. W. Nichols, R. B. Chevalier and J. R. Dwyer, *Nat. Commun.*, 2018, 9, 3278.

Paper

51 I. Capila and R. J. Linhardt, *Angew. Chem., Int. Ed.*, 2002, **41**, 390-412.

- 52 B. Mulloy, in *Heparin A Century of Progress*, ed. R. Lever, B. Mulloy and C. P. Page, Springer Berlin Heidelberg, Berlin, Heidelberg, 2012, vol. 207, pp. 77–98.
- 53 R. Linhardt, S. Murugesan and J. Xie, *Curr. Top. Med. Chem.*, 2008, 8, 80–100.
- 54 L. M. Longo, Y. Gao, C. A. Tenorio, G. Wang, A. K. Paravastu and M. Blaber, *Protein Sci.*, 2018, 27, 431–440.
- 55 P. Wong, B. Hampton, E. Szylobryt, A. M. Gallagher, M. Jaye and W. H. Burgess, *J. Biol. Chem.*, 1995, 270, 25805–25811.
- 56 W. H. Burgess, A. M. Shaheen, M. Ravera, M. Jaye, P. J. Donohue and J. A. Winkles, *J. Cell Biol.*, 1990, 111, 2129–2138.
- 57 X. Zhu, H. Komiya, A. Chirino, S. Faham, G. M. Fox, T. Arakawa, B. T. Hsu and D. C. Rees, *Science*, 1991, 251, 90–93.
- 58 X. Zhu, B. T. Hsu and D. C. Rees, Structure, 1993, 1, 27-34.
- 59 T. P. Bui, Y. Li, Q. M. Nunes, M. C. Wilkinson and D. G. Fernig, Selective labelling of arginine residues engaged in binding sulfatedglycosaminoglycans, *bioRxiv*, 2019, preprint, DOI: 10.1101/574947.

- 60 M. Tsutsui, Y. He, K. Yokota, A. Arima, S. Hongo, M. Taniguchi, T. Washio and T. Kawai, ACS Nano, 2016, 10, 803–809; M. Tsutsui, Y. He, K. Yokota, A. Arima, S. Hongo, M. Taniguchi, T. Washio and T. Kawai, ACS Nano, 2016, 10, 803–809.
- 61 C. Plesa, S. W. Kowalczyk, R. Zinsmeester, A. Y. Grosberg, Y. Rabin and C. Dekker, *Nano Lett.*, 2013, 13, 658–663.
- 62 C. J. Robinson, N. J. Harmer, T. L. Blundell and J. T. Gallagher, *Int. J. Exp. Pathol.*, 2004, **85**, A72–A72.
- 63 M. Ishihara, P. N. Shaklee, Z. Yang, W. Liang, Z. Wei, R. J. Stack and K. Holme, *Glycobiology*, 1994, 4, 451–458.
- 64 R. Raman, G. Venkataraman, S. Ernst, V. Sasisekharan and R. Sasisekharan, *Proc. Natl. Acad. Sci. U. S. A.*, 2003, **100**, 2357–2362.
- 65 S. Ye, Y. Luo, W. Lu, R. B. Jones, R. J. Linhardt, I. Capila, T. Toida, M. Kan, H. Pelletier and W. L. McKeehan, *Biochemistry*, 2001, 40, 14429–14439.
- 66 Y. M. N. D. Y. Bandara, J. Saharia, B. I. Karawdeniya, J. T. Hagan, J. R. Dwyer and M. J. Kim, *Nanotechnology*, 2020, 31, 335707.
- 67 Y. M. N. D. Y. Bandara, J. Saharia, B. I. Karawdeniya, P. Kluth and M. J. Kim, *Anal. Chem.*, 2021, 93, 11710– 11718.